Skin Temperature Measurement based on Human Skeleton Extraction and Infra-red Thermography

An Application of Sensor Fusion Methods in the Field of Physical Training

Julia Richter[1], Christian Wiede[1], Sascha Kaden[1], Martin Weigert[2] and Gangolf Hirtz[1]

[1]*Department of Electrical Engineering and Information Technology, Chemnitz University of Technology, Reichenhainer Str. 70, 09126 Chemnitz, Germany*

[2]*Department of Behavioural and Social Sciences, Chemnitz University of Technology, Reichenhainer Str. 70, 09126 Chemnitz, Germany*

Keywords: Infra-red Thermography, Skin Temperature, Sensor Fusion, Human Skeleton, Physical Training.

Abstract: Skin temperature measurements play a vital role in the diagnosis of diseases. This topic is also increasingly investigated for applications in the field of physical training. One of the limitations of state-of-the-art methods is the manual, time-consuming way to measure the temperature. Moreover, extant literature gives only little insight into the skin temperature behaviour after the training. The aim of this study was to design an automatic method to measure the skin temperature during and after training sessions for the biceps brachii. For this purpose, we fused thermal images and skeleton data to locate this muscle. We could successfully demonstrate the working principle and observed a temperature increase even several minutes after the end of the training. This study therefore contributes to the automation of skin temperature measurements. A transfer of our approach could be beneficial for other application fields, such as medical diagnostics, as well.

1 INTRODUCTION

Infra-red thermography plays an increasingly important role in a wide range of application fields. In medicine, it is a non-invasive diagnostic method to detect abnormal body temperatures, which are indicators for a variety of diseases, such as breast cancer and diabetic vascular disorder (Lahiri et al., 2012) or arthritis (Ring and Ammer, 2012). In sports medicine, infra-red thermography is applied to measure the degree of regeneration or to detect overuse reactions in order to avoid injuries (Hildebrandt et al., 2012).

Recently, researchers have shown an increased interest in the investigation of the relationship between skin temperature and muscle activity during training. To date, however, only few studies examined the temperature profile after training sessions. Moreover, the methods presented in previous work determined the skin temperature of a region in a manual way and are therefore time-consuming. The purpose of this study is to facilitate skin temperature determination of a certain region by introducing an automatic method. We fused images from a thermal camera as well as skeleton data from the Kinect sensor. For this, we have developed a calibration method that enables this sensor fusion. We demonstrated the working principle for the biceps brachii and analysed the heat development during and after the training with biceps curls. Therefore, this study makes a major contribution to research on the relationship between skin temperature and muscle activity in the field of sports science. At this point, we assumed that the muscle is not covered by clothes. The study has been organised as follows: Section 2 examines the extant literature on infra-red thermography and calibration. Section 3 begins by presenting the sensor system and the calibration procedure, including both intrinic and extrinsic calibration as well as the mapping process. Subsequently, this section explains the skin temperature measurement. Section 4 is concerned with the evaluation methodology, while Section 5 presents and discusses the results. We close the paper with conclusions and an outlook at future work in Section 6.

2 RELATED WORK

2.1 Infra-red Thermography

More recent attention has focused on the evaluation of surface temperature changes in training diagnos-

Richter J., Wiede C., Kaden S., Weigert M. and Hirtz G.
Skin Temperature Measurement based on Human Skeleton Extraction and Infra-red Thermography - An Application of Sensor Fusion Methods in the Field of Physical Training.
DOI: 10.5220/0006095100590066
In *Proceedings of the 12th International Joint Conference on Computer Vision, Imaging and Computer Graphics Theory and Applications (VISIGRAPP 2017)*, pages 59-66
ISBN: 978-989-758-227-1

tics. Variations in temperature can indicate the grade of muscle activity, which can be visualised by evaluating infra-red thermography images. In the following, existing literature is reviewed with the focus on the applied analysis methods.

Bartuzi et al. revealed statistically significant correlations between the skin temperature and EMG parameters for the biceps brachii by employing infrared thermography (Bartuzi et al., 2012). They adjusted a thermal camera in such a way that the captured thermal images showed only the muscle itself. The skin temperature was then determined using a special software that analysed manually defined regions. Formenti et al. examined the skin temperature development of the region that covers the calf muscle after standing calf raise exercises (Formenti et al., 2013). They observed an increasing skin temperature during and also two minutes after the exercise, which is an indicator that the active muscle emitted heat. Their temperature determination works semi-automatically: they manually selected a region of interest (ROI), which was located on the calf and then automatically determined the five warmest pixels. In the next step, they considered a region of five by five pixels around each of these warmest pixels and averaged them. This average was regarded as the final temperature for the previously selected ROI. Ludwig et al. thereupon verified a correlation between this very method and a method that simply averages the pixels belonging to the selected ROI (Ludwig et al., 2014).

Other approaches were based on anatomical information, which allowed the derivation of muscle locations in the thermal image. Two examples are the studies of Bandeira et al. and Neves et al.: according to the arrangement of the different muscles in the thigh, Bandeira et al. manually selected ROIs for temperature determination (Bandeira et al., 2012). In a similar manner, Neves et al. estimated the centre of the biceps brachii by exploiting the knowledge about the muscle anatomy (Neves et al., 2014).

Several methods employ markers that were attached to the skin. In this way, specific muscle temperatures were determined by manually evaluating the region between these markers in the recorded thermal images. Fröhlich et al., for example, bonded corks to a human body in order to measure temperatures belonging to various regions (Fröhlich et al., 2014), while Neves et al. fixed tapes to the biceps brachii. Further significant analyses and discussions on thermographic investigations, their techniques and influencing factors were presented in the works of Fernández et al. and Ring and Ammer (Fernández-Cuevas et al., 2015), (Ring and Ammer, 2015).

The evidence presented in this section suggest that there is need to investigate automatic methods for skin temperature evaluation. To date, automatic techniques to measure muscle temperature cannot be found in extant literature. Therefore, we propose such an automatic method that employs skeleton extraction algorithms to detect specific muscles. This enables an automatic localisation and analysis of specific muscle regions. Moreover, we demonstrated that after performing biceps curls, the temperature of the surface surrounding the biceps brachii increases, which supports the findings of Formenti et al.

2.2 Calibration

In order to combine skeletal data with thermal images, the Kinect version 1.0 skeleton joint coordinates and the images of the thermal camera had to be fused. For this procedure, a calibration of both sensors was required to allow a mapping of the thermal image to the Kinect RGB image, in which the skeleton joints are represented in 2-D coordinates.

The combination of a thermal camera and an RGB camera or a depth sensor, such as the Kinect, was widely used for different applications. Thomanek et al. implemented a pedestrian detection algorithm based on both RGB images and thermal images (Thomanek et al., 2011). On the one hand, pedestrians could be detected in thermal images even at night, when the detection on the RGB image failed. On the other hand, the detection in thermal image failed on warm days and under strong solar radiation. In these cases, however, pedestrians could be detected in the RGB image. The principle of compensating single sensor weaknesses was extended by Geschwandtner et al. (Gschwandtner et al., 2011). They utilised a thermal camera, a laser range scanner and an RGB camera in the field of autonomous driving. Other applications of thermal imaging in combination with other sensors are the maintenance of power equipment (Nakagawa et al., 2014), the building sector (Vidas et al., 2013) and e-rehabilitation (Richter et al., 2016). All these applications required a reliable calibration to fuse several optical systems to one combined world coordinate system. For this purpose, three aspects had to be considered: an adequate calibration target, whose pattern is detectable for every employed sensor, as well as the intrinsic and the extrinsic calibration.

In the visible light spectrum, a planar checkerboard is the commonly used calibration target. By detecting the inner checkerboard corners, information about distortions in the RGB images can be estimated. However, this working scheme is not applicable for

Figure 1: Sensor system with thermal camera and Kinect.

thermal images. Even if a checkerboard with appropriate material is illuminated by an infra-red heater, the edges of the checkerboard appear smoothed and cannot be accurately localised. To overcome this problem, alternative calibration targets have been developed. Nakagawa et al. proposed two plastic plates with inverse circular patterns (Nakagawa et al., 2014), which could be plugged into each other. For the calibration of a thermal and an RGB sensor, one plate was plugged onto the other and served as an isolating layer when they were heated. The isolating layer was then removed, so that only the heated circles were visible in the thermal image. At the same time, the circle boundaries could be detected in the RGB image as well. In comparison to that, Vidas et al. used a planar mask with cut-out squares, which was held in front of a backdrop with a different temperature (Vidas et al., 2013). With this method, checkerboard corners could more accurately detected than in case of the commonly used checkerboard calibration described above. Rangel et al. introduced a similar approach, but instead of squares, they cut out asymmetrical circles to increase the accuracy (Rangel et al., 2014). They heated this pattern to enable the circle detection in the thermal image. In contrast to the calibration of RGB sensors, the characteristic of this kind of thermal calibration targets is that the edges are blurred in the thermal image. The advantage of circles in such cases is a more stable detection: the centre of a circles can be detected more robustly than edges in such cases. While all these approaches used passive calibration targets, Ellmauthaler et al. suggested an LED grid (Ellmauthaler et al., 2013), whereas Gschwandtner et al. proposed a checkerboard with resistors as active calibration targets (Gschwandtner et al., 2011). An overview about different calibration targets was presented by Rangel et al. (Rangel et al., 2014).

The intrinsic calibration in all presented approaches was always performed according to the method of Zhang (Zhang, 2000), which assumed a pinhole camera model. Sections 3.2 and 3.3 present a detailed explanation of the intrinsic and extrinsic calibration procedures we applied in our study.

3 METHODS

This section presents the sensor system, the calibration steps and the procedure to measure the skin temperature.

3.1 Sensor System

The sensor system comprises an RGB-D sensor, i. e. a Kinect version 1.0, which additionally provides a human skeleton stream, and a thermal camera, i. e. a FLIR A35sc. The thermal camera has a thermal resolution of 50 mK. The spatial resolution of the sensor is 320×256 pixel. The rotation between both sensors was as small as possible, so that both sensors share approximately the same re-projection plane. The sensor system is illustrated in Figure 1.

3.2 Intrinsic Calibration

The aim of the camera calibration is the mapping of the thermal image onto the Kinect RGB image, in which the skeleton joints are represented in 2-D image coordinates.

For all calibration steps that are connected with the thermal sensor, we used an aluminium plate with cut-out circles, which is similar to Rangel et al. (Rangel et al., 2014). In contrast to Rangel et al., the circles on our target are symmetrically arranged, see Figure 2. Similar to Vidas et al. (Vidas et al., 2013), we used a TFT monitor as a backdrop that emits a different temperature, as illustrated in Figure 2. By using this calibration target, we could detect circles in the thermal image according to the algorithm by Suzuki and Abe (Suzuki and Abe, 1985).

The thermal camera was intrinsically calibrated using the method proposed by Zhang (Zhang, 2000). As a result, we obtained the camera matrix of the thermal camera $\mathbf{K}_{\text{therm}}$. The camera matrix $\mathbf{K}$ is generally defined as (Hartley and Zisserman, 2004):

$$\mathbf{K} = \begin{bmatrix} \alpha_x & s & p_x \\ 0 & \alpha_y & p_y \\ 0 & 0 & 1 \end{bmatrix} \tag{1}$$

This matrix contains the scale factors in x and y direction α_x and α_y, the skew s and the x and y coordinate p_x and p_y of the principal point.

In order to undistort the thermal image in radial and tangential direction, the method by Heikkila (Heikkila and Silven, 1997) was applied. The RGB images from the Kinect were not undistorted since there were almost no distortions. However, the Kinect was intrinsically calibrated to obtain the camera matrix of the RGB sensor $\mathbf{K}_{\text{RGB}}$. For this calibration,

we applied the commonly used checkerboard target. Both $\mathbf{K}_{\text{RGB}}$ and $\mathbf{K}_{\text{therm}}$ were needed for the extrinsic calibration and the mapping, which are described in the following sections.

3.3 Extrinsic Calibration

The calibration setup with the circle grid and the TFT monitor that has been introduced in Section 3.2 was used for the extrinsic calibration. Figure 2 shows the view of both RGB and thermal sensor. We eluded large rotations between the calibration target and the sensors, so that elliptical shapes and consequent false detections of the used circle detection algorithm could be avoided. The centre points of the circles that were detected in both RGB and undistorted thermal image and their 3-D correspondences were used for the extrinsic calibration that finally results in the rotation matrix $\mathbf{R}$ and the translation vector $\mathbf{t}$, see (Hartley and Zisserman, 2004). $\mathbf{R}$ and $\mathbf{t}$ are given with respect to the world coordinate system, which is located at the RGB sensor of the Kinect. In other words, $\mathbf{R}$ and $\mathbf{t}$ describe the rotation and translation of the thermal sensor with respect to the RGB sensor.

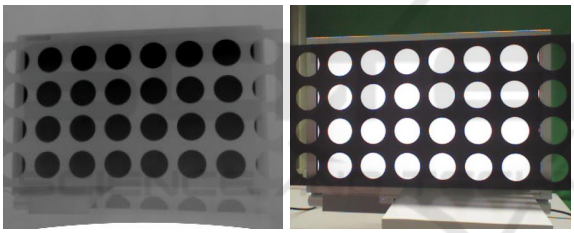

Figure 2: Calibration target in front of a TFT monitor, captured by the thermal camera (left) and the Kinect RGB camera (right).

In the next step, the undistorted thermal image could be mapped onto the RGB image by using the obtained camera matrices $\mathbf{K}_{\text{RGB}}$ and $\mathbf{K}_{\text{therm}}$, the rotation matrix $\mathbf{R}$ and the translation vector $\mathbf{t}$. This procedure is described in the following section.

3.4 Mapping

The mapping of the undistorted thermal image onto the RGB image comprised the back- projection of the undistorted thermal image to a plane in the world with a defined distance μ from the sensor using $\mathbf{K}_{\text{therm}}$, and the forward projection of the resulting world points to the RGB image using $\mathbf{K}_{\text{RGB}}$.

The back projection can be generally described as (Hartley and Zisserman, 2004):

$$\mathbf{X}(\mu) = \begin{pmatrix} M^{-1}(\mu\mathbf{x} - \mathbf{p}_4) \\ 1 \end{pmatrix}, \qquad (2)$$

Figure 3: Thermal data was mapped to the RGB image. The mapping result is shown in the present alpha-blended image.

whereas $\mathbf{X}(\mu)$ denotes the back-projected world point at the distance μ. In our application, μ was set to a value of 3 metres. M is the first 3×3 sub-matrix of the projection matrix $\mathbf{P}$. $\mathbf{p}_4$ is the fourth column of $\mathbf{P}$, which is generally defined as follows:

$$\mathbf{P} = \mathbf{K}\left[\mathbf{R}|\mathbf{t}\right] = \left[\mathbf{M}|\mathbf{p}_4\right] \qquad (3)$$

When we back-projected the thermal image to the world, $\mathbf{K}_{\text{therm}}$ was used to calculate the projection matrix $\mathbf{P}$. Since the world coordinate system was located at the RGB sensor, $\mathbf{R}$ and $\mathbf{t}$ that have been calculated during the extrinsic calibration were used for this back-projection step. The back-projected points from the thermal image $\mathbf{X}$ were then projected onto the RGB image according to Equation 4, which describes the general forward projection. At this point, $\mathbf{P}$ was calculated using $\mathbf{K}_{\text{RGB}}$ as well as a unit matrix for $\mathbf{R}$ and a zero vector for $\mathbf{t}$.

$$\mathbf{x} = \mathbf{P}\mathbf{X} \qquad (4)$$

The resulting coordinates $\mathbf{x}$ in the RGB image were afterwards bi-linearly interpolated. The forward projection was realised by means of a look-up-table. The result of this mapping process is exemplary illustrated in Figure 3.

3.5 Skeleton Extraction

We localised the biceps brachii muscle by means of the 2-D position of skeletal joints in the mapped images. For this purpose, we employed the skeleton extraction algorithm that is provided by the Kinect version 1.0 (Shotton et al., 2013). This algorithm calculates depth features from depth images and uses these features to train a randomised decision forest. With the help of this classifier, both 3-D and 2-D positions of overall 20 joints can be predicted. In our approach, we used only the 2-D elbow and the shoulder joints for the biceps brachii localisation on both left and right upper arm.

3.6 Skin Temperature Measurement

The biceps brachii temperature measurement using shoulder and elbow joints is illustrated in Figure 4.

We discovered that the original shoulder joints 5 and 9 were not suitable to accurately localise the biceps brachii. Therefore, their original locations were shifted by a parametrisable distance along the connecting, dashed line between the left and right shoulder in outward direction.

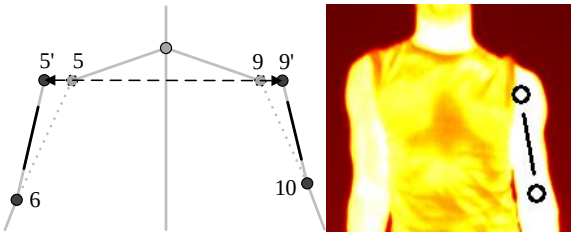

Figure 4: Left: Skin temperature measurement principle using shifted shoulder joints 5' and 9' and elbow joints 6 and 10. Joint indices are according to the Kinect indexing. Right: Thermal image with localised biceps brachii (black line).

In addition to this modification, we only used a parametrisable percentage of the pixels lying on the line connecting 5' and 6 or 9' and 10 respectively, staring symmetrically from the centre of this line. In this study, the percentage was set to 60 %, which results in a number of R and L temperature values for the right and left biceps brachii respectively. Finally, the skin temperature on the biceps brachii of the right arm $\vartheta_\mathrm{r}(t)$ and the left arm $\vartheta_\mathrm{l}(t)$ were calculated by determining the mean of the R and L temperature values of the pixels located on the black lines. These pixel values are denoted as $temp_\mathrm{r}(t)$ and $temp_\mathrm{l}(t)$ respectively, see Equation 5. t corresponds to the measurement point.

$$\vartheta_\mathrm{r}(t) = \frac{1}{R} \cdot \sum_{r=1}^{R} temp_\mathrm{r}(t) \tag{5a}$$

$$\vartheta_\mathrm{l}(t) = \frac{1}{L} \cdot \sum_{l=1}^{L} temp_\mathrm{l}(t) \tag{5b}$$

4 EVALUATION METHODOLOGY

In our experiments, we measured the biceps brachii temperature of the left and the right arm for four persons ($P = 4$) while they performed three sets of biceps curls with their right arm. The weight of the dumbbell was 7 kg. The distance from the camera was approximately 3 meters. The measurement schedule is presented in Table 1. At the beginning, each person had a time of 15 minutes for acclimatisation. The first measurement was taken directly after this acclimatisation phase ($t = 1$). Then every person had to perform as many biceps curls as possible for every set. Directly after each set, a measurement was performed ($t = 2,3,4$). The pause between two consecutive sets was 1 min. After the last set had been performed, nine further measurements were taken, whereas the time difference given in Table 1 is relative to the measurement with index t=4. The measurements for both arms were taken synchronously.

For evaluation, the measurements were equidistantly displayed, which means that the distance does not correspond to the time that elapsed between the measurement points.

We used three ways to generate temperature profiles. The first profile exemplarily displays the absolute temperature measured for the right arm $\vartheta_r(t)$ and left arm $\vartheta_l(t)$ of one of the probands, see Figure 5. For the second profile, see Figure 6, we aimed at visualising the averaged relative changes $\vartheta_{r,rel}(t)$ and $\vartheta_{l,rel}(t)$ with respect to the starting temperature t_0 of each arm, see Equations 6. The starting temperature corresponds to the measurement time $t = 1$, i. e. after acclimatisation. This type of representation was required for the evaluation of different probands' data to eliminate the influence of different environmental temperatures for the different probands.

$$\vartheta_{\mathrm{r,rel}}(t) = \frac{1}{P} \cdot \sum_{p=1}^{P} (\vartheta_\mathrm{r}(t) - \vartheta_\mathrm{r}(t_0)) \tag{6a}$$

$$\vartheta_{\mathrm{l,rel}}(t) = \frac{1}{P} \cdot \sum_{p=1}^{P} (\vartheta_\mathrm{l}(t) - \vartheta_\mathrm{l}(t_0)) \tag{6b}$$

The third profile illustrates the averaged difference between the right and the left arm for each measure-

Table 1: Measurement schedule.

Measurement Point t	Description
1	After acclimatisation
2	After first set
3	After second set
4	After third set
5	After 1 min
6	After 2 min
7	After 3 min
8	After 4 min
9	After 5 min
10	After 10 min
11	After 15 min
12	After 20 min
13	After 25 min

ment time and is defined as

$$\vartheta_{\text{diff}}(t) = \frac{1}{P} \cdot \sum_{p=1}^{P} \left(\vartheta_{\text{r}}(t) - \vartheta_{\text{l}}(t)\right) . \tag{7}$$

This profile type allows to eliminate environmental changes during a proband's training session and is visualised in Figure 7.

5 RESULTS AND DISCUSSION

In this section, the obtained temperature profiles that were described above are presented. The aim of these analyses is to investigate the difference between the temperature of the right biceps, which was active, and the left biceps, which was passive. We discuss every profile and explain occurring effects.

Absolute Temperatures of a Single Person. Figure 5 compares the absolute temperatures of the biceps of the right and the biceps of the left arm. From this figure, we can see that the temperature of the right biceps increases more than the temperature of the left biceps. What is interesting is that the maximal temperature of the active biceps was reached only several minutes after the training. These results are consistent with the findings of Formenti et al. (Formenti et al., 2013).

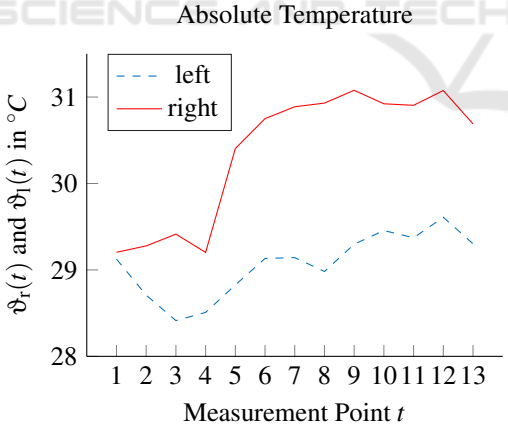

Figure 5: Absolute temperatures over time for one proband.

A possible explanation for this behaviour is that the cardiovascular system reacts to the physical stress by providing more blood to the active muscle. The blood has core body temperature, which results in the warming of the muscle. The adjacent tissue warms up as well due to thermal conduction. This described process needs time and results in the delay that is visible in the graph.

Temperatures Relative to the Starting Temperature of all Persons. To compare the temperature behaviour of the right and left biceps for more than one proband, we examined the mean relative temperature, see Figure 6. This type of evaluation allows the determination of temperature changes with respect to a start time. Taking the average of all probands, we obtained results that are comparable to the previous profile with one proband. Moreover, it can be seen that the temperature of the right arm increases by approximately 1.5 °C on average. The temperature of the left arm decreases slightly at the beginning. An explanation for this is that the blood flow might even be reduced in the passive arm.

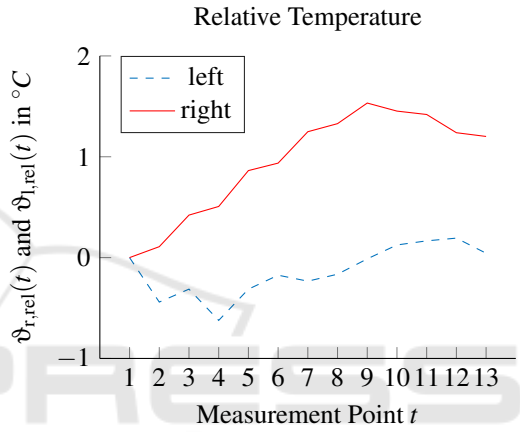

Figure 6: Mean relative temperature with respect to start temperature over time for all probands.

Temperature Difference Between Arms of all Persons. In order to eliminate environmental influences during one training session, we evaluated the mean difference between the temperatures of the right and the left arm. By doing this, eventual temperature changes in the training room would not influence the measurement, because this change would influence both arms. Moreover, by employing this evaluation method, we can determine the temperature difference compared to the corresponding limb, i. e. the left arm, which is passive. Figure 7 provides the according temperature profile.

The graph illustrates that, after the first set, the right arm has a higher temperature as the left arm. Another finding to emerge from this graph is that, averaged over all probands, the right arm is more than 1 °C warmer than the left arm at the maximum.

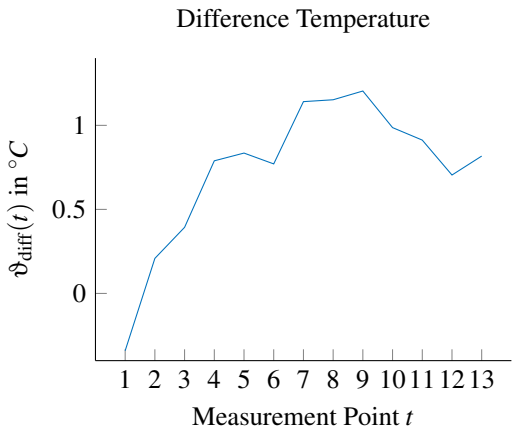

Figure 7: Mean temperature difference between right and left arm over time for all probands.

6 CONCLUSIONS AND FUTURE WORK

In this study, we presented a method to automatically determine and evaluate skin temperatures. This method is based on a sensor fusion of a thermal camera and the Kinect. In order to fuse both sensor data, we introduced a novel calibration procedure and designed a special calibration target. The obtained results provide further support for the hypothesis that the skin temperature increases during and after the training. Moreover, we evaluated relative temperature measurements, i. e. differences between active and passive muscles, instead of absolute measurements. This allows the elimination of environmental changes in a training session.

Further research could investigate the influence of subcutaneous fat tissue and clothing on the thermal conduction. Moreover, future research might explore skin temperature profiles of other muscles as well. Another aspect in our future work will be the detection of skeleton joints directly on the thermal image, which could considerably simplify the sensor system.

Continued efforts are needed to transfer our approach to other applications fields, such as medical diagnostics, which can profit from automatic temperature measurements.

ACKNOWLEDGEMENTS

This project is funded by the European Social Fund (ESF). We furthermore would like to express our thanks to all the persons who contributed to this project during the recordings.

REFERENCES

Bandeira, F., Moura, M. A. M. d., Souza, M. A. d., Nohama, P., and Neves, E. B. (2012). Can thermography aid in the diagnosis of muscle injuries in soccer athletes? *Revista Brasileira de Medicina Do Esporte*, 18(4):246–251.

Bartuzi, P., Roman-Liu, D., and Wiśniewski, T. (2012). The influence of fatigue on muscle temperature. *International Journal of Occupational Safety and Ergonomics*, 18(2):233–243.

Ellmauthaler, A., da Silva, E. A., Pagliari, C. L., Gois, J. N., and Neves, S. R. (2013). A novel iterative calibration approach for thermal infrared cameras. In *2013 IEEE International Conference on Image Processing*, pages 2182–2186. IEEE.

Fernández-Cuevas, I., Marins, J. C. B., Lastras, J. A., Carmona, P. M. G., Cano, S. P., García-Concepción, M. Á., and Sillero-Quintana, M. (2015). Classification of factors influencing the use of infrared thermography in humans: A review. *Infrared Physics & Technology*, 71:28–55.

Formenti, D., Ludwig, N., Gargano, M., Gondola, M., Dellerma, N., Caumo, A., and Alberti, G. (2013). Thermal imaging of exercise-associated skin temperature changes in trained and untrained female subjects. *Annals of biomedical engineering*, 41(4):863–871.

Fröhlich, M., Ludwig, O., Kraus, S., and Felder, H. (2014). Changes in skin surface temperature during muscular endurance indicated strain-an explorative study. *International Journal of Kinesiology & Sports Science*, 2(3):23.

Gschwandtner, M., Kwitt, R., Uhl, A., and Pree, W. (2011). Infrared camera calibration for dense depth map construction. In *Intelligent Vehicles Symposium (IV), 2011 IEEE*, pages 857–862. IEEE.

Hartley, R. I. and Zisserman, A. (2004). *Multiple View Geometry in Computer Vision*. Cambridge University Press, ISBN: 0521540518, second edition.

Heikkila, J. and Silven, O. (1997). A four-step camera calibration procedure with implicit image correction. In *Proceedings of the 1997 Conference on Computer Vision and Pattern Recognition (CVPR '97)*, CVPR '97, pages 1106–, Washington, DC, USA. IEEE Computer Society.

Hildebrandt, C., Zeilberger, K., Ring, E. F. J., and Raschner, C. (2012). *The application of medical infrared thermography in sports medicine*. INTECH Open Access Publisher.

Lahiri, B., Bagavathiappan, S., Jayakumar, T., and Philip, J. (2012). Medical applications of infrared thermography: a review. *Infrared Physics & Technology*, 55(4):221–235.

Ludwig, N., Formenti, D., Trecroci, A., Gargano, M., and Alberti, G. (2014). Comparison of image analysis methods in skin temperature measurements during physical exercise.

Nakagawa, W., Matsumoto, K., de Sorbier, F., Sugimoto, M., Saito, H., Senda, S., Shibata, T., and Iketani, A. (2014). Visualization of temperature change using

RGB-D camera and thermal camera. In *Workshop at the European Conference on Computer Vision*, pages 386–400. Springer.

Neves, E. B., Vilaça-Alves, J., Krueger, E., and Reis, V. M. (2014). Changes in skin temperature during muscular work: a pilot study. *Pan American Journal of Medical Thermology*, 1(1):11–15.

Rangel, J., Soldan, S., and Kroll, A. (2014). 3D thermal imaging: Fusion of thermography and depth cameras. In *International Conference on Quantitative InfraRed Thermography*.

Richter, J., Wiede, C., Apitzsch, A., Nitzsche, N., Lösch, C., Weigert, M., Kronfeld, T., Weisleder, S., and Hirtz, G. (2016). Assisted Motion Control in Therapy Environments Using Smart Sensor Technology: Challenges and Opportunities. In *Proceedings of Zukunft Lebensräume Kongress 2016*, pages 90–102.

Ring, E. and Ammer, K. (2012). Infrared thermal imaging in medicine. *Physiological measurement*, 33(3):R33.

Ring, E. and Ammer, K. (2015). The technique of infrared imaging in medicine. In *Infrared Imaging*. IOP Publishing.

Shotton, J., Girshick, R., Fitzgibbon, A., Sharp, T., Cook, M., Finocchio, M., Moore, R., Kohli, P., Criminisi, A., Kipman, A., et al. (2013). Efficient human pose estimation from single depth images. *Pattern Analysis and Machine Intelligence, IEEE Transactions on*, 35(12):2821–2840.

Suzuki, S. and Abe, K. (1985). Topological structural analysis of digitized binary images by border following. *Computer Vision, Graphics, and Image Processing*, 30(1):32–46.

Thomanek, J., Ritter, M., Lietz, H., and Wanielik, G. (2011). Comparing Visual Data Fusion Techniques Using FIR and Visible Light Sensors to Improve Pedestrian Detection. pages 119–125. IEEE.

Vidas, S., Moghadam, P., and Bosse, M. (2013). 3d thermal mapping of building interiors using an RGB-D and thermal camera. In *Robotics and Automation (ICRA), 2013 IEEE International Conference on*, pages 2311–2318. IEEE.

Zhang, Z. (2000). A flexible new technique for camera calibration. *IEEE Transactions on pattern analysis and machine intelligence*, 22(11):1330–1334.